



# Correlation between the histogram and power spectral density analysis of AFM and SKPFM images in an AA7023/AA5083 FSW joint

Zohreh Esfahani <sup>a, b, 1</sup>, Ehsan Rahimi <sup>c, 1</sup>, Madjid Sarvghad <sup>d</sup>, Ali Rafsanjani-Abbasi <sup>c</sup>,  
Ali Davoodi <sup>c, \*</sup>

<sup>a</sup> Materials and Polymers Engineering Department, Faculty of Engineering, Hakim Sabzevari University, Sabzavar, Iran

<sup>b</sup> Razi Metallurgical Research Center (RMRC), Tehran, Iran

<sup>c</sup> Materials and Metallurgical Engineering Department, Faculty of Engineering, Ferdowsi University of Mashhad, Mashhad, Iran

<sup>d</sup> Science & Engineering Faculty, Queensland University of Technology (QUT), Queensland, 4001, Australia

## ARTICLE INFO

### Article history:

Received 27 May 2017

Received in revised form

6 February 2018

Accepted 9 February 2018

Available online 10 February 2018

### Keywords:

Aluminum

FSW

AFM/SKPFM

Power spectral density

Corrosion

## ABSTRACT

Microstructural and Volta potential behavior of a friction stir welded dissimilar joint of AA7023 to AA5083 has been investigated. Interfacial regions were characterized by SEM-EDS, AFM, SKPFM and optical microscopy techniques. A quantitative correlation between corrosion data from histogram and power spectral density (PSD) analysis, which are related to Volta potential distribution, was established. PSD analysis of SKPFM images showed that the lowest Volta potential in the highest spatial frequency belongs to AA5083, while the highest Volta potential in lowest spatial frequency corresponds to intermetallic particles mainly on AA7023 matrix. Immersion test showed that intermetallic particles in the two matrices, and especially FSW interface, were susceptible to corrosion attack due to a high driving force between these surface constituents.

© 2018 Elsevier B.V. All rights reserved.

## 1. Introduction

Among various materials, aluminum and its alloys are of interest for various applications, particularly in automotive, aerospace, and ship industries. This is because of their low density, high strength and good corrosion performance [1–5]. 5XXX series of aluminum alloys, with magnesium as the principal alloying element, are favorable for their high strength, corrosion resistance in marine atmosphere, good formability, and weldability [6–9]. The corrosion behavior of AA5083 depends on microstructural features including grain size, second-phase size and the presence of intermetallic phases (IMPs). Although IMPs lead to enhanced mechanical properties, their presence could make the alloy susceptible to localized corrosion [6,7]. Different IMPs on AA5083 were already reported including  $Al_6(Fe, Mn, Cr)$ ,  $(Cr, Fe)Al_7$ ,  $(Mn, Fe)Al_6$ ,  $Mg_3Mn_2Al_{12}$ , and  $Al_6Mn$  [7,8,10]. Segregation of electrochemically active Mg–Al phases at grain boundaries has been reported to lead to stress corrosion cracking and inter-granular corrosion attack [7].

7xxx series alloys (Al–Zn–Mg–Cu) are popular for aircraft and aerospace structures because of their high strength-to-density ratio, good ductility, and excellent corrosion resistance in most media [8,11–13]. They rely on Zn as the primary alloying element which makes them excellent for fatigue applications. However, large amounts of alloying elements such as Zn and Mg could lead to brittleness and segregation, which in turn reduce mechanical properties and performance [14,15]. An alloy such as AA7075 shows poor corrosion resistance because of the presence of large amounts of IMPs which might be anodic or cathodic (relative to the matrix alloy). IMPs reported in AA7075 include  $MgZn_2$ ,  $Mg_2Si$ ,  $Al_3Fe$ ,  $Al_7Cu_2Fe$ ,  $Mg(AlCu)$  and  $Al_2CuMg$  [6,14–16].

Aluminum alloys are difficult to be welded by conventional methods such as the fusion welding due to hot cracking and porosity development after welding [17–20]. Friction stir welding (FSW) has been used to overcome problems related to fusing welding. FS welded joints show different zones in the weld including stirred zone (SZ), thermo-mechanically affected zone (TMAZ) and heat affected zone (HAZ) [17,20–22]. The microstructures of all these regions and IMPs are different from those of the base metal which in turn lead to different corrosion characteristics [4,23]. IMPs and the FSW interface play a major role in localized

\* Corresponding author.

E-mail address: [a.davodi@um.ac.ir](mailto:a.davodi@um.ac.ir) (A. Davoodi).

<sup>1</sup> These authors contributed equally to this manuscript.

corrosion especially in the initial stages of corrosion [2,24,25]. For this reason, a combination of topography analysis by Atomic Force Microscopy (AFM) in the air or in a solution and Volta potential mapping by Scanning Kelvin Probe Force Microscopy (SKPFM) in the air appears to be a powerful tool to study localized corrosion [5,26–28]. In fact, a linear correlation has been previously found between the corrosion potential of the metal and Volta potential values measured by SKPFM. Indeed, more noble materials show higher Volta potential values [29].

Histogram plots of Volta potential variations have been reported in our previous studies [4,6]. Although histogram plots could point to the presence, number and driving forces between the surface constituents, they do not provide information about the correlation between Volta potential values of roughness profiles and spatial frequency vector in the x-y plane. Accordingly, a more complementary description could be provided using Power Spectral Density (PSD) of Volta potential mapping. This allows Volta potential roughness to be compared over different spatial frequency ranges. In this paper, SKPFM has been employed together with AFM, optical microscopy (OM) and scanning electron microscopy (SEM-EDS) for a better understanding on the impact of FSW and IMPs on the corrosion behavior of aluminum alloys.

## 2. Experimental procedure

### 2.1. Welding procedure

A 5 mm thick plate of AA5083 alloy was friction stir butt-welded to a 7 mm thick AA7023 plate as discussed previously [6]. Chemical compositions of the materials used in this study are listed in Table 1.

### 2.2. Sample preparation

In order to provide a suitable sample for OM, SEM-EDS and AFM/SKPFM measurements, a cut-off cross-section from the weld was degreased in acetone, mechanically wet polished down to 0.05  $\mu\text{m}$  using alumina slurry and then washed by ethanol and finally dried by hot air blow. For AFM and SKPFM, a mirror-like polished surface was used to avoid contamination. For microstructural characterization, the sample was etched for 20 s in Keller's etchant ( $190 \text{ H}_2\text{O} + 5 \text{ HNO}_3 + 3 \text{ HCl} + 2 \text{ HF}$ ).

### 2.3. Microscopical characterization

Morphology and microstructural characterization was carried out using a SEM (1450 VP, LEO) equipped with Energy Dispersive Spectroscopy of the X-ray (EDS) analysis.

### 2.4. AFM/SKPFM measurement

Volta potential mappings of the polished sample surface including the FSW region and aluminum matrices around it were achieved using AFM/SKPFM measurements. SKPFM mapping of the polished samples was performed to evaluate the relative nobility of IMPs and weld interface in the two alloys and FSW region. AFM and Volta potential images obtained using a commercial Solver Next AFM instrument (NT-MDT Company) from polished samples. All

mappings were acquired in air at the ambient temperature under the controlled relative humidity of  $\sim 35\%$ . The AFM tip was an n-type antimony doped, pyramid single crystal silicone coated by conductive PtIr (25 nm) and a Cr adhesive layer (2.5 nm). Dual-scan mode was carried out for the acquisition of surface potential mapping. In the first scan, topography data was recorded using the tapping mode technique. In the second step of the scan process (for Volta potential mapping), a lift scan height of about 10–20 nm was chosen (depending on the surface roughness) to avoid the topography impact on the Volta potential mapping. Topography and Volta potential were scanned with a pixel resolution of  $512 \times 512$  and scan rate of 0.3 Hz.

## 2.5. Corrosion investigation

To study the corrosion attack, the same polished sample was immersed in a 3.5 wt% NaCl corrosive solution for 20 min. After this time, the sample was washed with ethanol and finally dried by hot air blow.

## 3. Results and discussion

### 3.1. Microstructural analysis

Microstructural features of the weld area have been previously discussed in detail [6]. Notable notice from the previous work is the presence of Zn and the formation of Al-Mg-Zn compounds in the interface. Correspondingly, three areas consisting of AA7023, AA5083 and the interfacial region with different compositions were detected. Cu-rich particles which have been shown to make AA7xxx alloys susceptible to localized corrosion in marine media were also detected [14]. The composition difference (concentration gradient) in these areas was found responsible for the formation of galvanic couples or providing driving forces for corrosion [6]. Fig. 1 illustrates particles dispersed in the two adjacent matrices of AA7023 and AA5083 alloys. Coarse particles in AA5083 matrix (Fig. 1b and d) have been previously reported to be  $\text{Al}_6(\text{Mn}, \text{Fe})$  [24,30].

Stirring action during FSW may lead to the fragmentation or aggregation of  $\text{Al}_6(\text{Fe}, \text{Mn})$  particles. Therefore, the combination of stirring and heat gradient during FSW is supposed to affect the size of particles [6]. In addition, coarse IMPs of Al-Fe-Cu-Si type in the matrix of AA7023 which have been reported to be  $\text{Al}_3(\text{FeCuSi})$ , are shown in Fig. 1a and c [14]. The main corrosion attack is focused on the alloy matrix surrounding these IMPs through the formation of galvanic cells leading to the formation of pits. In this case, reduction of oxygen as the cathodic reaction of oxygen reduction occurs on intermetallic surfaces as more noble phases through the following reaction [24]:



The dissolution of Al occurs adjacent to the IMPs due to the weak oxide film in this region according to the following reaction [24]:



**Table 1**

Chemical composition of the friction stir welded Aluminum alloys (wt%).

Alloys	Mg	Zn	Mn	Cu	Fe	Si	Cr	Ti	Sn	Pb	Ni	Ca	Al
AA7023	2.127	4.227	0.138	1.353	0.943	0.836	0.077	0.015	0.007	0.089	0.018	0.01	bal
AA5083	5.349	0.112	0.491	0.138	0.33	0.088	0.064	0.013	0.003	–	–	–	bal

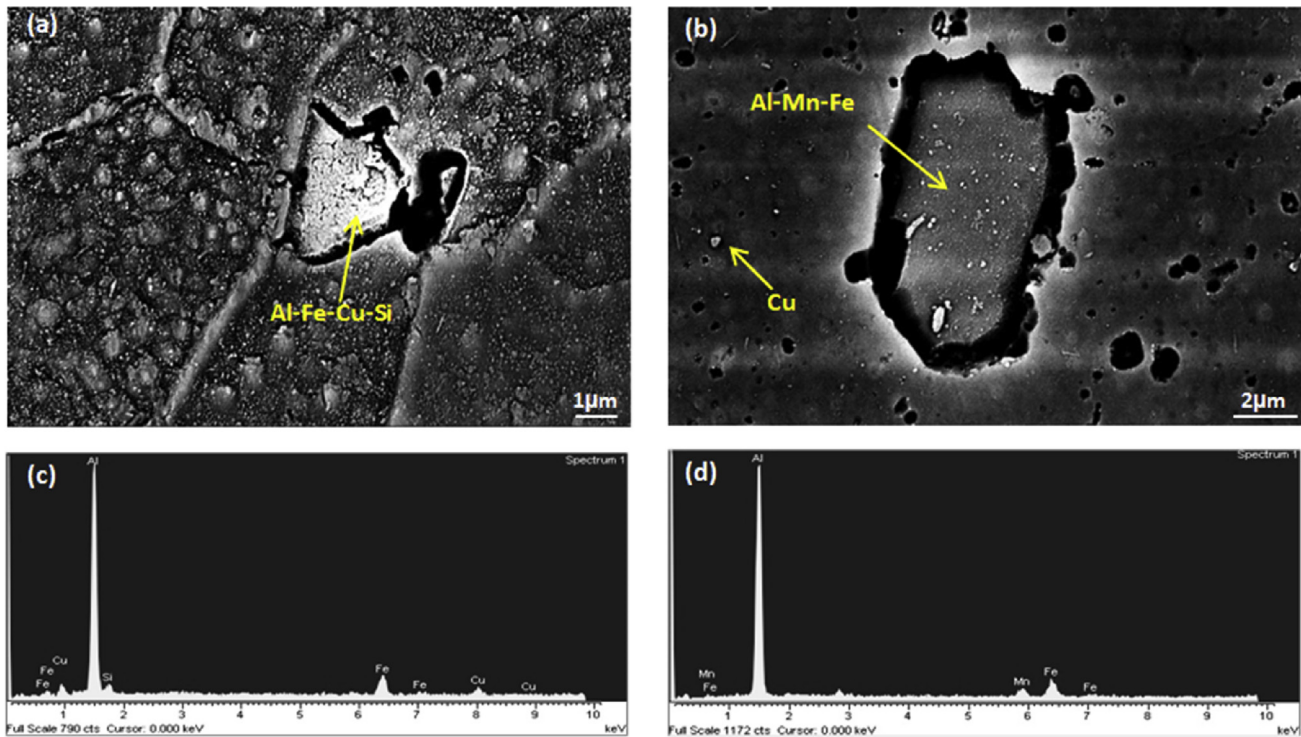


Fig. 1. SEM-EDS micrographs of intermetallic particles in the mixed region (stirred zone).

Another possibility, as one of the most commonly identified IMPs in high strength Al alloys, is the formation of  $Al_7Cu_2Fe$  which has a more positive dissolution potential than the Al matrix and hence can form a galvanic cell for pitting corrosion [24,26].

### 3.2. Topography and Volta potential measurements

To evaluate the relative nobility of IMPs in both Al alloys, SKPFM measurements were performed to map Volta potential variation on the prepared sample surface. In SKPFM method, AC and DC bias voltages are applied between a cantilever tip and the sample. The induced electrostatic force is detected and used to control  $V_{DC}$  such that the tip-sample potential difference is compensated [31]. Therefore, recording  $V_{DC}$  of the tip over the sample surface makes the mapping of the distribution of Volta potentials possible [29,31,32].

Fig. 2 shows topography and Volta potential mappings of the FSW interface in the dissimilar joint of both Al alloys. As shown in Fig. 2a, the topography image shows a uniform distribution of both Al alloys' heights with the roughness root-mean-square (RMS) of 54 nm. Fig. 2b shows an SKPFM image of the two separate regions around the weld interface (AA7023 on top and AA5083 at the bottom of the image).

Variably sized IMPs in AA7023 show higher Volta potential distribution compared to AA5083 due to the chemical composition variation in AA7023 [25,30]. In addition, the AA5083 region shows more uniform Volta potential distribution compared to AA7023. IMPs can be seen on the AA7023 surface (Fig. 1a); i.e. Al-Cu-Fe-Si containing particles with the highest Volta potential values. On the other hand, IMPs in AA5083 are mostly of Al-Mn-Fe type and pure Cu containing particles, as shown in Fig. 1b. Naturally, the solubility of alloying elements such as Mn, Cu, Fe, Mg, and Si in the alloy matrix has an influence on the reduction of Volta potential difference between IMPs and Al alloy matrices [7,14].

A common way to study topography and Volta potential data is

employing line profiles through potential mappings [33–36]. Therefore, histogram method provides more information about the Volta potential distribution of constitutive phases, as reported previously [4,6]. The deconvolution of Volta potential or topography histograms into multimodal Gaussian was calculated as below [4,6]:

$$Y = \frac{1}{\sigma\sqrt{\frac{\pi}{2}}} \exp\left[-\frac{2(x-\mu)^2}{\sigma^2}\right] \quad (3)$$

where  $Y$  represents the counts number,  $\sigma$  is the standard deviation,  $\mu$  is the mean potential value of Volta potential and  $x$  is Volta potential or topography values. As mentioned above, AFM and especially SKPFM images have been analyzed using image processing and histogram analysis. Table 2 shows the extracted key parameters from Volta potential histogram (Figs. 2d and 5a-c).

In order to accurately evaluate the spatial frequency of phases (particles sizes) with the Volta potential mapping, the PSD evaluation method was used. The method provides information related to the roughness of the component as a function of spatial frequency through the equation below [37–40]:

$$PSD(f) = \lim_{A \rightarrow \infty} \frac{1}{A} \left| \int_A z(r) \exp(-2\pi i f \cdot r) dr \right|^2 \quad (4)$$

where  $z(r)$  represents the Volta potential data of the surface roughness,  $A$  is the surface area of the measuring field,  $r$  is position vector and  $f$  is spatial frequency vector in the  $x-y$  plane. Histogram of SKPFM mapping (Fig. 2d) shows three peaks including AA5083 region, AA7023 region and FSW interface with the mean potential values ( $\mu$  or  $V_m$ ) of 66.1 mV (the lowest Volta potential), 244.5 mV and 366.6 mV (the highest Volta potential), respectively. The difference between the mean potential values is equivalent to

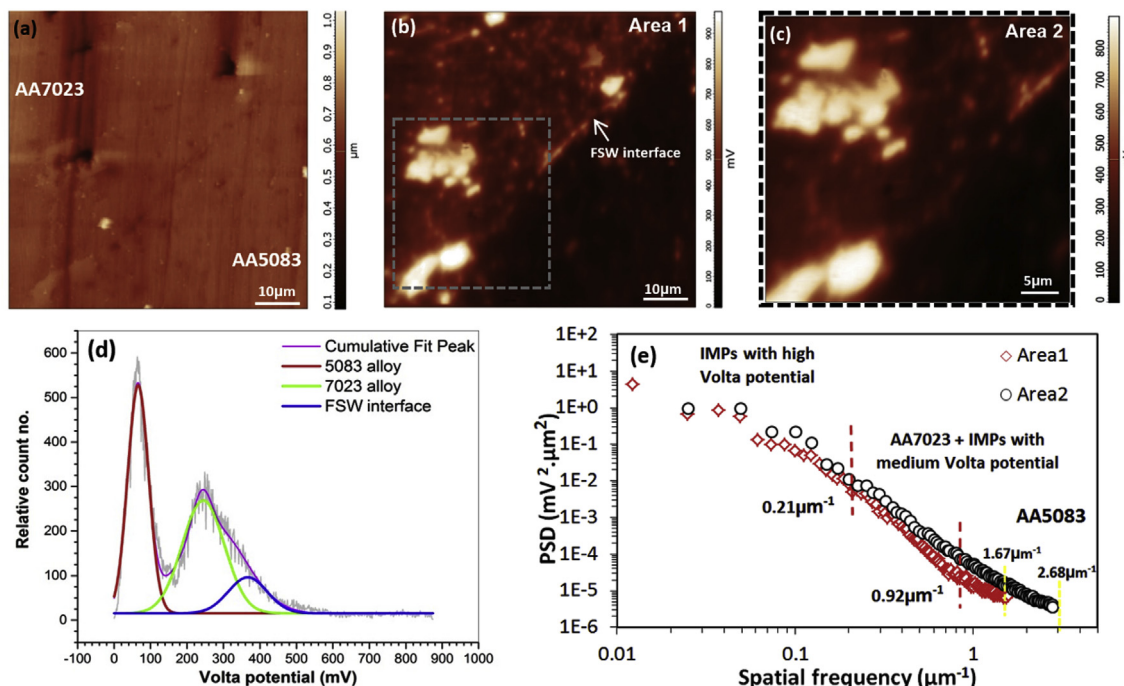


**Fig. 2.** (a, b) AFM topography and SKPFM image of the same FSW region, (c) greater magnification of b, (d) Histogram plot of SKPFM image in b, (e) PSD profiles of the FSW sample calculated from SKPFM images in b and c.

**Table 2**

Extracted Gaussian distribution parameters from Volta potential histograms.

Region label	Constituents	Mean value of Volta potential ( $\mu$ , mV)	Standard deviation of Volta potential ( $\sigma$ , mV)
Fig. 2d	Alloy 5083	66.1	28.8
	Alloy 7023	244.5	58.1
	FSW interface	366.6	53.3
Fig. 5a	Alloy 5083	30.2	14.2
	Alloy 7023	182.4	34.8
	FSW interface	282.2	46.2
Fig. 5b	IMPs	374.4	22.1
	Alloy 5083	59.8	34.6
	Alloy 7023	246.5	43.7
	FSW interface	346.9	26.2
Fig. 5c	IMPs	425.4	46.3
	Alloy 5083	55.6	20.2
	Alloy 7023	257.7	82.1
	FSW interface	475.7	61.8

driving force ( $\Delta V_m$ ) for micro-galvanic localized corrosion [4,41]. Galvanic corrosion may initiate in the FSW interface with  $\Delta V_m = 178.4$  mV between AA7023 and AA5083. Also, some IMPs on AA7023 matrix have Volta potentials similar to the FSW interface. Thus, the potential difference between the FSW interface and IMPs with  $\Delta V_m = 300.5$  mV could provide driving force for micro-galvanic corrosion. In fact, IMPs on AA7023 behave as cathode zones with respect to the base alloy.

Fig. 2e shows the PSD profiles of Volta potential mappings in two different scanned areas which are related to Fig. 2b (Area1) and Fig. 2c (Area 2). In the PSD profile, the lowest and highest spatial frequencies are related to the highest and lowest Volta potentials. Therefore, the higher spatial frequency is related to AA5083 region and lower value corresponds to the FSW interface and IMPs with high Volta potentials on AA7023. IMPs with high Volta potential distribution show lower spatial frequency than the IMPs with the lower values, as shown in Fig. 3. Therefore, three areas could be attributed to individual regions. These regions have been

determined on the basis of changes in the slope of PSD profile [42,43]. In other words, non-uniform scattering (PSD curves are non-linear) in PSD profiles is not due to the distribution but the different sizes of particles and phases in both base metals [38].

PSD of Area 2 shows higher spectral Volta potential than Area 1 over the spatial frequency which is due to the high Volta potential roughness of Area 2. IMPs with high Volta potential on AA7023 are mostly large sized (low frequency) which are placed after the spatial frequency of  $0.21 \mu\text{m}^{-1}$ . The spatial frequency in the range of  $0.21 \mu\text{m}^{-1} - 0.92 \mu\text{m}^{-1}$  is related to AA7023 and IMPs with medium Volta potential values. Moreover, Area 2 has one order frequencies more than Area 1 (the yellow lines in the frequency range of  $1.67 \mu\text{m}^{-1} - 2.68 \mu\text{m}^{-1}$ ). It can be concluded that the less distribution of Volta potential roughness is in AA5083 matrix. Fig. 4 shows SKPFM survey images of the FSW interface and IMPs in Al alloys from the upper region (7023 alloy) to middle region and finally into the lower region (5083 alloy). In addition, the FSW interface shows higher Volta potentials compared to the parent Al

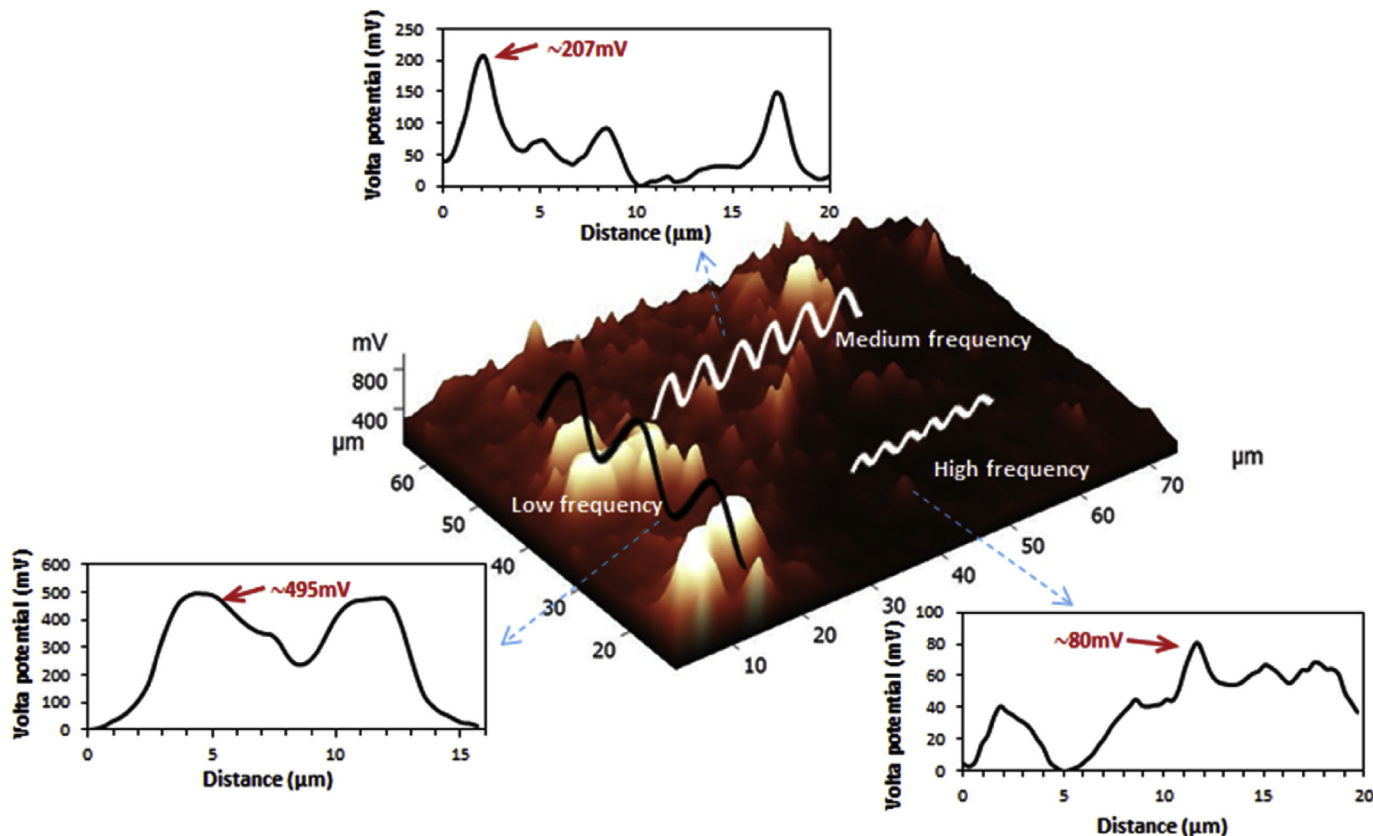


Fig. 3. Correlation between Volta potential distribution and spatial frequency for surface constituents corresponding to Fig. 2b (three line profiles were shown to confirm these results).

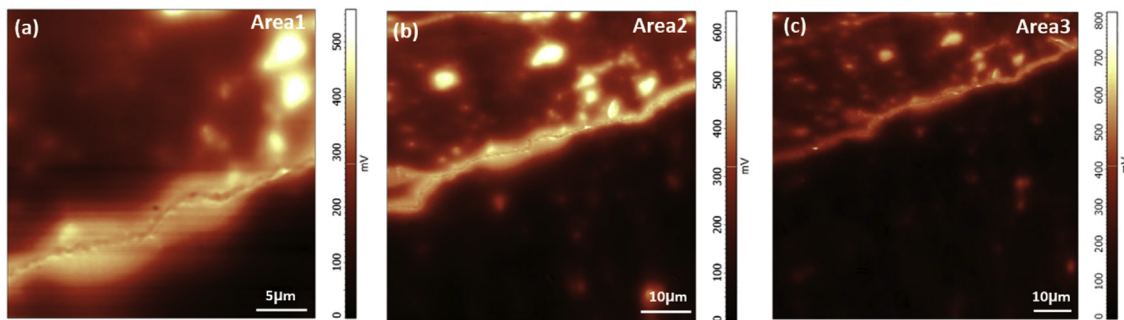


Fig. 4. (a, b, c) Survey of SKPFM Volta potential images of the FSW interface in AA7023 (upper region) and AA5083 (lower region) matrices.

alloys. It could be attributed to the formation of some noble precipitates in the FSW interface especially Al-Mg-Zn, as reported previously [6]. Thus, this region in contact with a corrosive media could be susceptible to galvanic attack [23].

Fig. 5 shows histogram and PSD analysis of survey SKPFM mappings of Fig. 4. Four different regions are detectable on the histogram analysis of SKPFM mappings in Areas 1, 2, and 3. By sweeping from the AA7023 to the middle area and then into AA5083, gradual increase and reduction are detectable in the histogram peaks of AA5083 and AA7023, respectively. In addition, by decreasing in AA7023 scanning surface area and moving into AA5083, a reduction can be seen in the peak intensity of FSW interface and IMPs, as shown in Fig. 5. These changes in histogram peaks can be clearly observed in Fig. 4a–c and also can be detected in PSD profiles data in Fig. 5d.

PSD in Fig. 5d shows the Volta potential distribution of components (phases and particles in both Al alloys) versus spatial frequencies (distribution of particles sizes) related to SKPFM mappings in Fig. 4a–c. During the survey from AA7023 to AA5083, a reduction occurs in the spatial frequency of AA5083 from  $7.8 \mu\text{m}^{-1}$  to  $1.9 \mu\text{m}^{-1}$ . This reduction has been attributed to the increase in Volta potential roughness in AA5083 matrix which could be confirmed by root-mean-square ( $\text{RMS}_{\text{Area 1}} = 0.108 \text{ mV} < \text{RMS}_{\text{Area 2}} = 0.132 \text{ mV} < \text{RMS}_{\text{Area 3}} = 0.138 \text{ mV}$ ). Another reduction is detectable in the frequency ranges of  $1.42 \mu\text{m}^{-1}$  to  $0.15 \mu\text{m}^{-1}$  which could be attributed to reduction in the distribution of IMPs with the medium Volta potential and surface area in AA7023. This reduction is clearly visible in the histogram analysis of SKPFM images in Fig. 5. In addition, a gradual reduction can be observed after  $1.42 \mu\text{m}^{-1}$  frequency which could

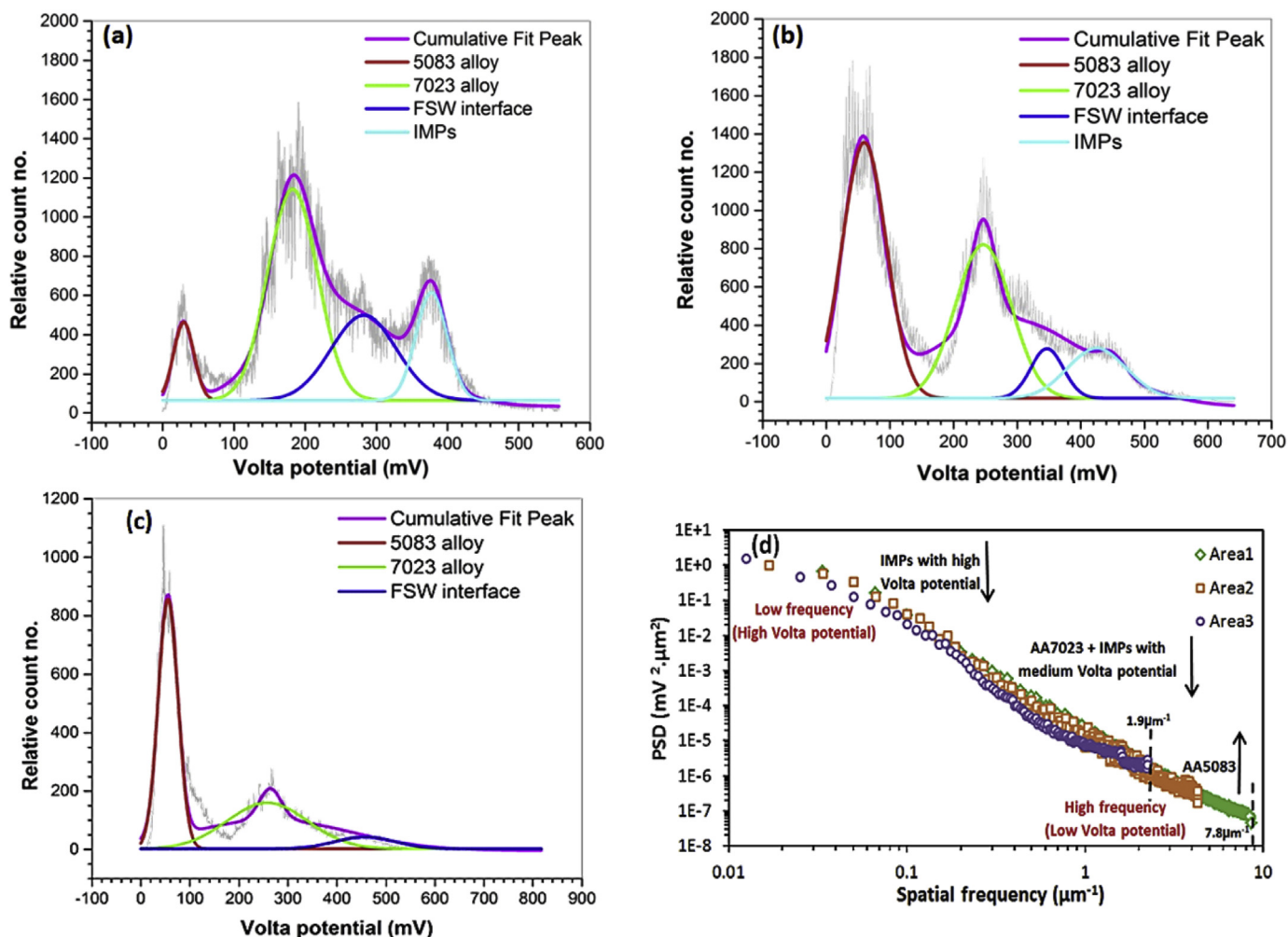


Fig. 5. (a,b,c) Histogram plots of three SKPFM images in Fig. 4a–c. (d) PSD profiles in a wide frequency range corresponding to SKPFM images in Fig. 4a–c.

be attributed to the reduction of IMPs distribution with the high Volta potential (Fig. 4b and c).

### 3.3. Correlation between AFM/SKPFM analysis and localized corrosion attack

To verify the corrosion initiation sites predicted by SKPFM analysis, OM images were captured from the sample with the polished surface after exposure to 3.5 %wt NaCl for 20 min, as shown in Fig. 6d and f. Moreover, Fig. 6a–c shows 3D SKPFM images and cross-sectional Volta potential analyses which are related to the pre-exposure test. SKPFM image shows a large potential gradient through the FSW interface between AA7023 and AA5083 measured by cross-sectional analysis (Fig. 6b). This suggests that these regions could be more susceptible to galvanic corrosion during exposure to corrosive electrolytes.

Line profile in Fig. 6b shows a high Volta potential difference between the two Al alloys with 138 mV driving force. As a result, a predominant attack is detectable on the FSW interface (Fig. 6d). A slightly more extended of corrosion attack towards AA5083 can be observed which could be due to the higher Volta potential difference between AA5083 and FSW (with a driving force of 372 mV) compared to that of AA7023 and FSW (with a driving force of 234 mV) as shown in Fig. 6d. These differences are related to variations in alloying elements [41,44], as reported in SEM-EDS result in

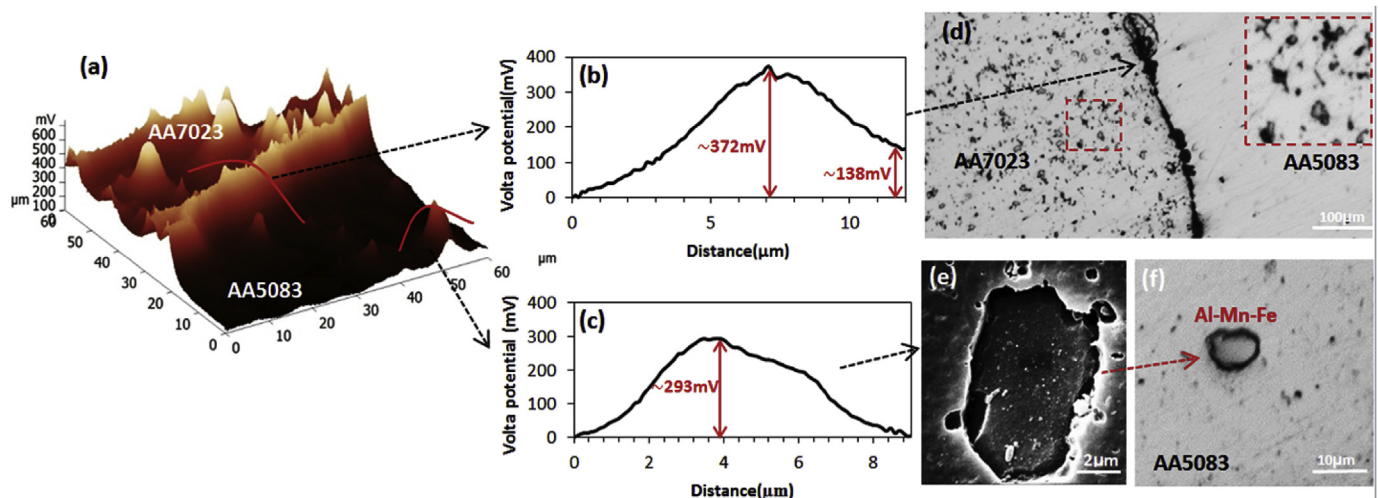
the previous work [6]. On the other hand, IMP detachment is detectable around galvanic couples between the IMPs and AA7023 matrix (shown more clearly in Fig. 6d). It can be concluded that alloying elements play an important role in the corrosion initiation, especially pitting corrosion due to the different compositions of IMPs and matrices as reported in Fig. 1 and through our previous work [6,41].

Fig. 6 shows a correlation between SKPFM/line profile and BSE-SEM images of Al-Mn-Fe particles on 5083 before exposure. Fig. 6f shows an OM image of Al-Mn-Fe particles after exposure to the corrosive media for 20 min. A black ring (corroded area) is observed around the Al-Mn-Fe particle due to the high Volta potential difference (293 mV) between IMPs and AA5083 matrix, Fig. 6c. In fact, amounts of Mg in AA5083 and the presence of Mn and Fe (as shown in Fig. 1b) provide a potential site for localized corrosion attack.

## 4. Conclusion

The interfacial region of a friction stir welded dissimilar joint of AA7023 and AA5083 was investigated using optical microscopy, SEM-EDS, and AFM/SKPFM techniques. The main conclusions are:

1. Correlation between histogram and power spectral density analysis was well explained by survey SKPFM mappings around the weld interface.



**Fig. 6.** (a) SKPFM image of the FSW sample before immersion in the corrosive media, (b, c) Line profile of the FSW interface and IMPs with high Volta potentials in AA5083 matrix obtained from SKPFM image, (d) optical microscopy image of the sample surface after 20 min immersion in 3.5%wt NaCl corrosive solution showing localized corrosion attack on the interface and IMPs in AA7023 (higher magnification of IMPs on AA7023 side is provided by the inserted image), (e) SEM image of an Al-Mn-Fe IMP before exposure to the corrosive media, (f) Optical image of the corroded IMP on the AA5083 side after 20 min immersion in 3.5 %wt NaCl corrosive solution.

- AA5023 region shows a lower PSD value in the high spatial frequencies compared to AA7023 with higher PSD values at low spatial frequency.
- PSD analysis showed that IMPs with highest Volta potentials on AA7023 matrix have the lowest spatial frequencies and vice versa.
- It was observed that localized corrosion initiated from the FSW interface, IMPs with high Volta potentials on AA7023 and (Al-Mn-Fe)-rich particles on the AA5083 matrix due to the great driving force values.

## Acknowledgments

Hakim Sabzevari University, Sabzevar, Iran is acknowledged for providing AFM/SKPFM experimental facilities. Ferdowsi University of Mashhad, Mashhad, Iran and Queensland University of Technology (QUT), Australia are appreciated for providing optical microscopy and SEM facilities.

## References

- Q. Zheng, X. Feng, Y. Shen, G. Huang, P. Zhao, Effect of plunge depth on microstructure and mechanical properties of FSW lap joint between aluminum alloy and nickel-base alloy, *J. Alloys Compd.* 695 (2017) 952–961.
- L. Lacroix, L. Ressler, C. Blanc, G. Mankowski, Combination of AFM, SKPFM, and SIMS to study the corrosion behavior of S-phase particles in AA2024-T351, *J. Electrochem. Soc.* 155 (2008) C131–C137.
- N. Devarajan, G. Sivaswamy, R. Bhattacharya, D.P. Heck, M.A. Siddiq, Complex incremental sheet forming using back die support on aluminium 2024, 5083 and 7075 alloys, *Proc. Eng.* 81 (2014) 2298–2304.
- M. Sarvghad-Moghaddam, R. Parvizi, A. Davoodi, M. Haddad-Sabzevar, A. Imani, Establishing a correlation between interfacial microstructures and corrosion initiation sites in Al/Cu joints by SEM-EDS and AFM-SKPFM, *Corrosion Sci.* 79 (2014) 148–158.
- L. Lacroix, L. Ressler, C. Blanc, G. Mankowski, Statistical study of the corrosion behavior of Al<sub>2</sub>Cu/Mg intermetallics in AA2024-T351 by SKPFM, *J. Electrochem. Soc.* 155 (2008) C8–C15.
- A. Davoodi, Z. Esfahani, M. Sarvghad, Microstructure and corrosion characterization of the interfacial region in dissimilar friction stir welded AA5083 to AA7023, *Corrosion Sci.* 107 (2016) 133–144.
- K. Yasakau, M. Zheludkevich, M. Ferreira, Lanthanide salts as corrosion inhibitors for AA5083. Mechanism and efficiency of corrosion inhibition, *J. Electrochem. Soc.* 155 (2008) C169–C177.
- S. Hosseini-pour, An investigation into hot deformation of aluminum alloy 5083, *Mater. Des.* 30 (2009) 319–322.
- S.S. Mirjavadi, M. Alipour, S. Emamian, S. Kord, A. Hamouda, P.G. Koppad, R. Keshavamurthy, Influence of TiO<sub>2</sub> nanoparticles incorporation to friction stir welded 5083 aluminum alloy on the microstructure, mechanical properties and wear resistance, *J. Alloys Compd.* 712 (2017) 795–803.
- R.E. Clegg, Measurements of the interface between 5083 aluminium and liquid mercury using impedance spectroscopy, *Corrosion Sci.* 52 (2010) 4028–4034.
- O. Hatamleh, P.M. Singh, H. Garmestani, Corrosion susceptibility of peened friction stir welded 7075 aluminum alloy joints, *Corrosion Sci.* 51 (2009) 135–143.
- J.C. Bertonecello, S.M. Manhabosco, L.F. Dick, Corrosion study of the friction stir lap joint of AA7050-T76511 on AA2024-T3 using the scanning vibrating electrode technique, *Corrosion Sci.* 94 (2015) 359–367.
- J. Pang, F. Liu, J. Liu, M. Tan, D. Blackwood, Friction stir processing of aluminium alloy AA7075: microstructure, surface chemistry and corrosion resistance, *Corrosion Sci.* 106 (2016) 217–228.
- Q. Meng, G. Frankel, Effect of Cu content on corrosion behavior of 7xxx series aluminum alloys, *J. Electrochem. Soc.* 151 (2004) B271–B283.
- J. Shin, T. Kim, D. Kim, K. Kim, Castability and mechanical properties of new 7xxx aluminum alloys for automotive chassis/body applications, *J. Alloys Compd.* 698 (2017) 577–590.
- S.-S. Wang, G. Frankel, J.-T. Jiang, J.-F. Chen, S.-L. Dai, L. Zhen, Mechanism of localized breakdown of 7000 series aluminum alloys, *J. Electrochem. Soc.* 160 (2013) C493–C502.
- K. Kumar, S.V. Kailas, On the role of axial load and the effect of interface position on the tensile strength of a friction stir welded aluminium alloy, *Mater. Des.* 29 (2008) 791–797.
- F. Cioffi, J. Ibáñez, R. Fernández, G. González-Doncel, The effect of lateral offset on the tensile strength and fracture of dissimilar friction stir welds, 2024Al alloy and 17% SiC/2124Al composite, *Mater. Des.* (1980-2015) 65 (2015) 438–446.
- F. Zhang, X. Su, Z. Chen, Z. Nie, Effect of welding parameters on microstructure and mechanical properties of friction stir welded joints of a super high strength Al–Zn–Mg–Cu aluminum alloy, *Mater. Des.* 67 (2015) 483–491.
- S. Sinhar, D. Dwivedi, Enhancement of mechanical properties and corrosion resistance of friction stir welded joint of AA2014 using water cooling, *Mater. Sci. Eng. A* 684 (2017) 413–422.
- M. Esmaily, N. Mortazavi, W. Osikowicz, H. Hindsefelt, J.-E. Svensson, M. Halvarsson, G. Thompson, L.-G. Johansson, Influence of multi-pass friction stir processing on the corrosion behavior of an Al-Mg-Si alloy, *J. Electrochem. Soc.* 163 (2016) C124–C130.
- U. Donatus, G.E. Thompson, X. Zhou, Anodizing behavior of friction stir welded dissimilar aluminum alloys, *J. Electrochem. Soc.* 162 (2015) C657–C665.
- M. Esmaily, N. Mortazavi, W. Osikowicz, H. Hindsefelt, J. Svensson, M. Halvarsson, G. Thompson, L. Johansson, Corrosion behaviour of friction stir-welded AA6005-T6 using a bobbin tool, *Corrosion Sci.* 111 (2016) 98–109.
- K.A. Yasakau, M.L. Zheludkevich, S.V. Lamaka, M.G. Ferreira, Role of intermetallic phases in localized corrosion of AA5083, *Electrochim. Acta* 52 (2007) 7651–7659.
- N. Birbilis, R. Buchheit, Electrochemical characteristics of intermetallic phases in aluminum alloys an experimental survey and discussion, *J. Electrochem. Soc.* 152 (2005) B140–B151.
- C. Senöz, S. Borodin, M. Stratmann, M. Rohwerder, In situ detection of differences in the electrochemical activity of Al<sub>2</sub>Cu IMPs and investigation of

- their effect on FFC by scanning Kelvin probe force microscopy, *Corrosion Sci.* 58 (2012) 307–314.
- [27] D.B. Blücher, J.-E. Svensson, L.-G. Johansson, M. Rohwerder, M. Stratmann, Scanning kelvin probe force microscopy a useful tool for studying atmospheric corrosion of MgAl alloys in situ, *J. Electrochem. Soc.* 151 (2004) B621–B626.
- [28] M. Jönsson, D. Thierry, N. LeBozec, The influence of microstructure on the corrosion behaviour of AZ91D studied by scanning Kelvin probe force microscopy and scanning Kelvin probe, *Corrosion Sci.* 48 (2006) 1193–1208.
- [29] M. Rohwerder, F. Turcu, High-resolution Kelvin probe microscopy in corrosion science: scanning Kelvin probe force microscopy (SKPFM) versus classical scanning Kelvin probe (SKP), *Electrochim. Acta* 53 (2007) 290–299.
- [30] R. Buchheit, A compilation of corrosion potentials reported for intermetallic phases in aluminum alloys, *J. Electrochem. Soc.* 142 (1995) 3994–3996.
- [31] K. Honbo, S. Ogata, T. Kitagawa, T. Okamoto, N. Kobayashi, I. Sugimoto, S. Shima, A. Fukunaga, C. Takatoh, T. Fukuma, Visualizing nanoscale distribution of corrosion cells by open-loop electric potential microscopy, *ACS Nano* 10 (2016) 2575–2583.
- [32] C. Barth, A.S. Foster, C.R. Henry, A.L. Shluger, Recent trends in surface characterization and chemistry with high-resolution scanning force methods, *Adv. Mater.* 23 (2011) 477–501.
- [33] R.I. Revilla, J. Liang, S. Godet, I. De Graeve, Local corrosion behavior of additive manufactured AlSiMg alloy assessed by SEM and SKPFM, *J. Electrochem. Soc.* 164 (2017) C27–C35.
- [34] N. Sathirachinda, R. Pettersson, J. Pan, Depletion effects at phase boundaries in 2205 duplex stainless steel characterized with SKPFM and TEM/EDS, *Corrosion Sci.* 51 (2009) 1850–1860.
- [35] N. Sathirachinda, R. Pettersson, S. Wessman, J. Pan, Study of nobility of chromium nitrides in isothermally aged duplex stainless steels by using SKPFM and SEM/EDS, *Corrosion Sci.* 52 (2010) 179–186.
- [36] C. Örnek, J. Walton, T. Hashimoto, T. Ladwein, S. Lyon, D. Engelberg, Characterization of 475 C embrittlement of duplex stainless steel microstructure via scanning kelvin probe force microscopy and magnetic force microscopy, *J. Electrochem. Soc.* 164 (2017) C207–C217.
- [37] M. Senthilkumar, N. Sahoo, S. Thakur, R. Tokas, Characterization of micro-roughness parameters in gadolinium oxide thin films: a study based on extended power spectral density analyses, *Appl. Surf. Sci.* 252 (2005) 1608–1619.
- [38] P. Dash, P. Mallick, H. Rath, A. Tripathi, J. Prakash, D. Avasthi, S. Mazumder, S. Varma, P. Satyam, N. Mishra, Surface roughness and power spectral density study of SHI irradiated ultra-thin gold films, *Appl. Surf. Sci.* 256 (2009) 558–561.
- [39] M. Flemming, L. Coriand, A. Duparré, Ultra-hydrophobicity through stochastic surface roughness, *J. Adhes. Sci. Technol.* 23 (2009) 381–400.
- [40] E. Rahimi, A. Davoodi, A.R. Kiani Rashid, Characterization of screw dislocation-driven growth in nickel micro-nanostructure electrodeposition process by AFM, *Mater. Lett.* 210 (2018) 341–344.
- [41] A. Davoodi, J. Pan, C. Leygraf, S. Norgren, The role of intermetallic particles in localized corrosion of an aluminum alloy studied by SKPFM and integrated AFM/SECM, *J. Electrochem. Soc.* 155 (2008) C211–C218.
- [42] S. Chandran, S. Dold, A. Buvignier, K.-S. Krannig, H. Schlaad, G.n. Reiter, R. Reiter, Tuning morphologies of Langmuir polymer films through controlled relaxations of non-equilibrium states, *Langmuir* 31 (2015) 6426–6435.
- [43] E. Rahimi, A. Rafsanjani-Abbasi, A. Davoodi, A. Kiani-Rashid, Shape evolution of water and saline droplets during icing/melting cycles on superhydrophobic surface, *Surf. Coatings Technol.* 333 (2018) 201–209.
- [44] A. Davoodi, J. Pan, C. Leygraf, R. Parvizi, S. Norgren, An insight into the influence of morphological and compositional heterogeneity of an individual intermetallic particle on aluminium alloy corrosion initiation, *Mater. Corros.* 64 (2013) 195–198.